Analyst

ROYAL SOCIETY OF CHEMISTRY

PAPER

View Article Online
View Journal | View Issue

Check for updates

Cite this: *Analyst*, 2025, **150**, 5043

Optical characterization of a nanogel–nanostar plasmonic nanocomposite for microfluidic sensing and surface-enhanced Raman scattering

Casey Folks, Nishka Ghiloria and Laura D. Casto-Boggess *

Plasmonic nanoparticles embedded in polymer matrices combine the exceptional optical properties of plasmonic nanoparticles with the versatile mechanical and chemical characteristics of polymers, enabling robust and functional surface-enhanced Raman scattering (SERS) detection platforms for chemical sensing. SERS has become one of the most powerful analytical techniques due to the electromagnetic and chemical enhancement of plasmonic nanoparticles, realizing enhancement factors up to 12 orders of magnitude. In particular, gold nanostars are highly efficient and sensitive SERS facilitators due to the extreme near-field enhancement that arises from their sharp tips and branches, commonly referred to as 'hotspots'. Self-assembling phospholipid nanogels that exhibit thermally reversible pseudoimmobilization properties offer a unique opportunity for designing biocompatible plasmonic nanocomposites with thermally responsive viscosity profiles. Hence, a thermally responsive plasmonic nanocomposite was designed by embedding gold nanostars in a phospholipid nanogel. Remarkably, this nanogel–nanostar composite can be reversibly immobilized in microfluidic channels for SERS analysis and then flushed out of the channel for reuse of the microchannel. The optical properties of gold nanostars were analyzed to characterize the reliability and sensitivity of the nanogel–nanostar composite for SERS sensing and detection applications. Finally, the nanogel–nanostar composite was applied to SERS analysis in a microfluidic device, demonstrating a low nanomolar detection performance for rose bengal dye.

Received 5th August 2025,
Accepted 2nd October 2025

DOI: 10.1039/d5an00833f

rsc.li/analyst

Introduction

Raman spectroscopy is a non-destructive and powerful spectroscopic technique that uses molecular vibrations to provide structurally specific spectral information for chemical identification.[1] However, the efficiency of Raman scattering is intrinsically low, limiting high-sensitivity detection capabilities. Over the past few decades, surface-enhanced Raman spectroscopy (SERS) has evolved into one of the most important and powerful analytical techniques in optical spectroscopy due to its exceptionally high sensitivity and selectivity.[2–4] The SERS effect is extremely dependent on the interaction between analyte molecules with the surface of plasmonic nanoparticles. SERS takes advantage of the localized surface plasmon resonance (LSPR) of nanoparticles, resulting in an enhancement of the local electric near field around the surface of plasmonic nanoparticles.[4–6] In particular, gold nanoparticles of different morphologies have been used in a variety of spectroscopic applications like SERS and dark-field spectroscopy (DFS) for sensing and imaging.[7–9]

The LSPR of gold nanoparticles can be modulated by changing their size, shape, and surrounding dielectric medium. Gold nanoparticles have been extensively studied for the development of SERS substrates due to their unique optical properties and biocompatibility, resulting in high analytical sensitivity and specificity.[4,9,10] Variations in SERS intensity across different morphologies arise from the number of intrinsic hotspots per particle, where nanostars provide the most hotspots due to their sharp tips and protruding branches.[11] Hotspot formation is a key component for realizing strong SERS enhancement.[12] Gold nanostars possess distinct optical properties that make them excellent SERS substrates, with enhancements surpassing those of traditional gold nanoparticles by more than two orders of magnitude.[5,13–15]

SERS is an exceptional optical detection method that affords molecular structural information while also exhibiting extreme sensitivity that rivals fluorescence.[4,6,16,17] However, practical application is limited due to poor reliability, thus prompting efforts to develop consistent and cost-effective SERS substrates for routine use.[18,19] Colloidal substrates offer affordability, reproducible synthesis, and easily tailored optical performance, but reliable hotspot formation remains difficult, leading to inconsistent signal enhancements.[15] These inconsistencies compromise the accuracy and reliability of measure-

---

Department of Chemistry, The University of North Carolina at Charlotte, Charlotte, NC 28223, USA. E-mail: lcastobo@charlotte.edu

ments in Raman detection. In contrast, solid substrates, including roughened metal surfaces or metal nanoparticles immobilized on solid supports, afford a more stable analyte detection platform.[19,20] However, solid substrate utilization often involves dry analysis, where acquisition occurs after drop-casting the analyte. Unfortunately, this method lacks uniform or obvious analyte distribution patterns after drying, especially for more dilute samples, making micro-Raman detection challenging.[19,21]

Plasmonic nanocomposites offer revolutionary potential for SERS applications, enabling more robust, but highly flexible platforms. Plasmonic nanoparticles incorporated with polymers synergistically benefit from the excellent optical properties of nanoparticles and the wide range of mechanical and chemical properties of polymers.[22] Successful translation of these materials into practical applications, however, requires scalable, reproducible fabrication methods that allow for precise control over particle aggregation, distribution uniformity, and optical behavior.[9] Specifically, in the design of nanocomposites, gold nanostars are favorable because their sharp branches and hot spots provide plasmonic coupling inside the polymer matrix, which enables significant enhancement of Raman signals.[22,23] Careful attention to tunable design parameters, polymer identity, and nanoparticle density has shown the capability to boost the reliability of plasmonic polymer nanocomposites as SERS substrates.[9]

Microfluidic SERS detection approaches have previously been reported.[24–27] Self-assembling phospholipid structures offer a unique opportunity for designinga microfluidic biocompatible plasmonic nanocomposite with a thermally responsive viscosity profile. Mixtures of long-chain and short-chain phospholipids like DMPC (1,2-dimyristoyl-*sn-glycero*-3-phosphocholine) and DHPC (1,2-dihexanoyl-*sn-glycero*-3-phosphocholine) produce self-assembling nanostructures such as discs and wormlike bicelles (Fig. 1).[28] The morphology of nanostructures is dependent on the concentration of phospholipids in solution, temperature, and the ratio of DMPC to DHPC (*q*-ratio).[29,30] The tunable physicochemical properties of DMPC-DHPC enable a switch between high viscosity and low viscosity with a narrow change in temperature. The thermal responsiveness of DMPC-DHPC enables plasmonic nanoparticles to be pseudo-immobilized as they self-assemble into entangled nanoworms at temperatures above 23 °C (Fig. 1). Since the thermal switching is completely reversible, the nanogel can be disentangled back to low viscosity with cooling. This reversible behavior is leveraged for microfluidic applications where the low viscosity mixture is loaded into a fluidic system, pseudo-immobilized above 23 °C, and then cooled back down to rinse the phospholipid mixture out of the microfluidic system entirely.[31,32]

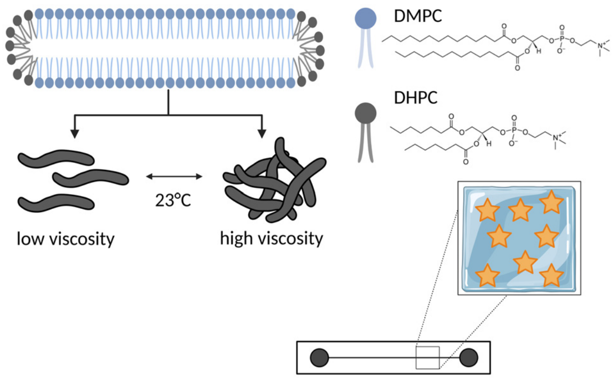

Fig. 1 1,2-Dimyristoyl-*sn-glycero*-3 phosphocholine (DMPC) and 1,2-dihexanoyl-*sn-glycero*-3-phosphocholine (DHPC), at low viscosity with self-assembling worm-like structures and high viscosity with intertwined worms above 23 °C. DMPC-DHPC nanogel is embedded with gold nanostars and introduced into a microfluidic channel for analysis at 25 °C as an erasable SERS sensing platform.

Here, we have created a thermally responsive plasmonic nanocomposite with optical tunability using gold nanostars embedded in DMPC-DHPC phospholipid nanogel as a SERS substrate. Through a mild change in temperature, the substrate can be reversibly immobilized for analysis in microfluidic channels and then flushed out of the channel for reuse of the device. Optical properties of gold nanogel–nanostar composites were analyzed and compared against nanogel-free nanostar suspensions to characterize the influence of nanogel encapsulation on optical property preservation. Furthermore, the viability of utilizing the nanogel–nanostar composite as a SERS substrate was demonstrated in a microfluidic platform, affording higher reproducibility than nanogel-free nanostar suspensions. In addition to improved uniformity of SERS activity, the potential to regenerate the SERS-active zone *via* gel dissolution and reloading presents a practical advantage for microfluidic SERS applications.

Materials & methods

Reagents and materials

Gold(III) chloride trihydrate, sodium citrate tribasic dihydrate, gold chloride solution, hydrochloric acid (1.0 N), L-ascorbic acid, silver nitrate ($AgNO_3$), and rose bengal were purchased from Sigma-Aldrich (St Louis, MO, USA). Thiol-functionalized methoxy poly(ethylene glycol) (mPEG-SH) 2000 was purchased from Nanocs Inc. (New York, NY, USA). Ethanol (Koptec), acetic acid solution (1.0 M) from Ward's Science, Sylgard 184 Silicone Elastomer Base, and Sylgard 184 Silicone Elastomer Curing Agent were purchased from VWR International (Suwanee, GA, USA). 1,2-Dimyristoyl-*sn-glycero*-3-phosphocholine (DMPC) and 1,2-dihexanoyl-*sn-glycero*-3-phosphocholine (DHPC) were purchased from Avanti Polar Lipids Inc. (Alabaster, AL, USA). Sodium acetate was purchased from Fisher Scientific (Fisher Scientific Co LLC, Hanover Park, IL, USA). DLP Craftsman Resin (ANYCUBIC, Shenzhen, China) was purchased from Amazon. Type 1 ultra-pure water prepared in an Elga PureLab System (Elga, Veolia Water Technologies Inc., Woodridge, IL, USA) was used for all sample preparation and syntheses. Prior to synthesis, the magnetic stir bars and glassware used in gold nanoparticle syntheses were cleaned with aqua regia.

Phospholipid nanogel preparation

Phospholipid nanogels were prepared according to a previously reported method.[33–35] DMPC and DHPC were weighed out with DMPC : DHPC *q*-ratio of 2.5. Filtered 50 mM sodium acetate buffered to pH = 4.5 was added to give a final lipid concentration of 20% (w/v), and the sample was vortexed until dissolved. Then, three freeze–thaw cycles were completed, followed by centrifugation at 10 000 rpm for 10 min at 4 °C. The preparations were aliquoted and stored at −20 °C until ready for use.

Gold nanostar synthesis and characterization

Nanostars were synthesized with an LSPR wavelength maximum ($\lambda_{\max}$) to align in resonance with a 638 nm laser excitation. The gold nanostar synthesis was performed using a modified version of a protocol described previously by De Silva Indrasekara *et al.*[13] For the seed mediated growth of surfactant-free gold nanostars, citrate capped gold nanospheres were synthesized using a modified version of the Turkevich method.[36] Briefly, in a 20 mL glass scintillation vial (VWR) containing a small magnetic stir bar, 10 mL of ultrapure water was added and stirred at 600 rpm to form a steady vortex. Under ambient conditions, 492 μL of gold chloride solution (5.08 mM) was added and mixed for 10 s. Then, 20 μL of HCl (1.0 N) was added and mixed for 10 s. Immediately following, 140 μL of spherical gold nanoparticles (synthesis and characterization is provided in the SI) was added and mixed for 10 s. Next, 34 μL of $AgNO_3$ (3.0 mM) was added and mixed for 5 seconds. Immediately after the addition of $AgNO_3$, the formation of gold nanostars begins, which is confirmed by a noticeable color change from colorless to navy blue. Thereafter, 100 μL of ascorbic acid (100 mM) was added and mixed for 60 s. Lastly, for long-term stability, 40 μL of mPEG-SH-2000 (1.0 mg mL^{-1}) was added and mixed for 10 min. The gold nanostars were purified by centrifugation at 3000*g* for 10 min, and the resultant pellet was resuspended in 3.0 mL of ultrapure water and stored at 4 °C. The stock solution of gold nanostars had an LSPR $\lambda_{\max}$ at 648 nm, an absorbance of 2.1, and a concentration of 0.229 nM. The calculation of gold nanostars concentration is provided in the SI. Nanoparticle morphology was evaluated using a JEOL JEM 2100 LaB_6 transmission electron microscope (TEM). A total of 8.0 μL of diluted nanoparticles was drop-cast onto a carbon-coated copper grid from Electron Microscopy Sciences (Hatfield, PA, USA). Four fields of view were used for size analysis using ImageJ. Size calculations and distributions for the average core diameter, branch length, and tip-to-tip size is shown in the SI.

Enhanced darkfield scattering (DFS) microscopy and hyperspectral imaging

The optical properties of gold nanostars embedded in DMPC-DHPC phospholipid nanogel were analyzed using DFS imaging under hyperspectral conditions. HORIBA Scientific's XploRA Raman microscope system integrated with Cytoviva's hyperspectral imaging spectrometer was used for single-particle analysis. Nanocomposites were prepared by mixing 5 μL of water and 20 μL of gold nanostars with 25 μL of phospholipid nanogel. The mixture was vortexed for 1 min and stored at 4 °C until ready to use. Colloidal gold nanostars were prepared in a 2 : 3 ratio of sodium acetate, pipette mixed, and then drop-cast for imaging. Final nanostar density was between 10^7–10^8 nanostars per microliter. For imaging, 8 μL of the sample was dropped on a glass slide, covered with a coverslip, and sealed with clear CoverVibe nail polish. Micro-Manager, an open-source microscopy software, was used to acquire at least three fields of view for a total of at least 1000 particles, with an exposure time of 200 ms using a 60× oil objective.[37] Spatial and spectral information of the enhanced dark-field hyperspectral image was obtained using Environment for Visualization (ENVI) 4.8 software (Cytoviva, Auburn, AL). Cytoviva's particle filter tool was used to analyze the spectral dimensions for each field of view to exclude aggregate and impurity contributions. Particles containing less than 1000 counts and greater than 5000 counts were excluded. Further, particles were spatially excluded that were larger than 20 pixels. To ensure consistency in nanogel viscosity, no more than the equivalent of three full scans (696 × 696 pixels) were acquired for each nanocomposite aliquot, to prevent sample drying or overheating. All dark field images were taken at 25 °C. Single-particle analysis, including the Kolmogorov–Smirnov test, the empirical cumulative distribution function, and probability density function, was carried out using Python toolkits including pandas, matplotlib, NumPy, and SciPy (scipy.stats).

Microfluidic chip fabrication

Microfluidic channels were cast into polydimethylsiloxane (PDMS) using soft lithography and 3D printed molds. A casting mold with twelve parallel 200 × 200-micron channels (L = 1.5 cm) was 3D printed using DLP Craftsman resin (gray) on an AnyCubic Photon DLP resin printer. The mold was UV cured for 30 min and baked overnight at 60 °C. Sylgard 184 and curing agent were mixed in a 1 : 10 ratio, poured into the printed mold, left to sit for approximately 2 hours until bubble-free, and then the PDMS was cured at 60 °C overnight. After the PDMS microchannel slab was released from the mold, the PDMS surface and a silicon wafer were rinsed thoroughly with detergent and water. Both substrates were then blown dry with argon gas and placed into a plasma chamber (PDC-001-HP, Harrick, Ithaca, NY). The vacuum was pulled down to 350 mTorr, and the plasma was turned on high power for 35 s. The timer was started once plasma generation was verified from a purple color observed through the chamber window. After exposure, both substrates were removed from the chamber and immediately brought into contact for permanent bonding of the PDMS microchannels to a silicon wafer. The final microdevice and microchannel image can be found in the SI.

Surface-enhanced Raman scattering (SERS) detection

Raman and SERS measurements were carried out using HORIBA Scientific's XploRA Raman microscope system. Horiba LabSpec6 software was used for SERS analysis using a 638 nm laser (16 mW), 10× objective, 600 grooves per mm grating, slit size of 200 µm, pinhole size of 100 µm, for five accumulations and an acquisition time of 10 s. Given this optical configuration, approximately 60 nanostars would be present in the SERS detection volume for a uniformly dispersed mixture. Samples were prepared by mixing rose bengal and gold nanostars in a 1 : 4 ratio. Next, the solution was diluted to half its original volume by lipid nanogel (q = 2.5) to deliver final concentrations of 10% total lipid and 40, 27, 20, 10, and 5 nM rose bengal. Background subtraction and peak analysis were performed using LabSpec6 (version 6.3) (Horiba Scientific, Edison, NJ) and Origin(Pro), version 2024, (OriginLab Corporation, Northampton, MA). Details are included in the SI. Measurements were carried out in a single microfluidic channel. The chilled sample pre-mixed with nanogel was loaded into the channel using a 1 mL syringe with a polypropylene syringe adaptor (OD 1.7 mm; ID 0.5 mm; L = 55 mm; LabSmith, Livermore, CA). After sample loading, the chip was placed on the microscope stage and allowed to come to 25 °C before measurement. Samples were measured in triplicate in at least 5 different locations within the channel. After each sample, the microchannel was rinsed with isopropanol and water.

Results & discussion

Characterization of colloidal gold nanostars

The optical properties of plasmonic nanoparticles heavily rely on their shape and size. The morphology of the synthesized gold nanostars (Fig. 2a) is characterized by their sharp tips protruding from a spherical core, with an average tip-to-tip diameter of 77.12 ± 13.69 nm. The LSPR $\lambda_{\max}$ of the gold nanostars was 648 nm (2.1 a.u, 0.229 nM) (Fig. 2b), which agrees well with previously reported seed-mediated and surfactant-free gold nanostar synthesis and characterization.[13] DFS under hyperspectral imaging was used to characterize the scattering properties of individual gold nanostars at the single-particle level prior to integration into phospholipid nanogels (Fig. 2c). It is of utmost importance to understand and characterize the optical scattering properties of single gold nanostars before incorporating into different matrices. Understanding how the optical behavior and performance at the single particle level is influenced by matrix type is important for SERS substrate development. DFS works by excluding unscattered incident light and utilizing incoming reflected light to provide an image on a dark background, thereby eliminating background noise typically experienced with bright-field microscopy.[38] Hyperspectral imaging provides spatial and spectral information about individual particles.[39] Hyperspectral data cubes are made up of two spatial dimensions and a spectral dimension. The spatial dimensions are viewed as a darkfield scattering image (Fig. 2c), while the spectral dimension affords scattering spectra for each pixel (examples in Fig. 2d). Combining DFS and hyperspectral imaging enables the single-particle scattering analysis of plasmonic nanoparticles to assess optical properties, in contrast to the ensemble measurement from UV-Vis spectroscopy shown in Fig. 2b. This allows isolation of nanoparticle scattering from background scattering and absorption from aggregates or impurities, which will not contribute to SERS enhancement mechanisms. The Cytoviva particle filter tool was used to facilitate the removal of aggregates and impurities by excluding particles that fall outside the range of 1000–5000 counts and are larger than 20 pixels. The deviation of scattering intensities over individual particles is attributed, in part, to variations in morphological features, such as different branch lengths. Three-dimensional structure and morphological heterogeneity can lead to plasmon broadening or multidirectional scattering.[40,41] The single-particle scattering spectra of individual gold nanostars show $\lambda_{\max}$ of 610 ± 33 nm (n = 1058) (Fig. 2d), which is blue-shifted from the bulk solution ensemble measurement. This highlights the importance of single particle scattering analyses, where background scatter and impurities are removed in opposition to ensemble UV-Vis measurements.

Optical property stabilization for gold nanostars embedded in thermally responsive nanocomposites

Plasmonic nanocomposites for SERS sensing and detection rely heavily on the optical properties of nanoparticles. The plasmon distribution and $\lambda_{\max}$ for gold nanostars are a representation of the stability and aggregation status of nanoparticles in the surrounding matrix.[9,42] As such, the influence of the nanogel matrix on nanoparticle stability and optical performance is essential. Fig. 3 presents the optical properties of gold nanostars embedded in nanogel. A hyperspectral DFS image and particle filtered image of the designed thermally responsive plasmonic nanocomposite are provided in Fig. 3a and b, respectively. After spatial and spectral filtering, scattering spectra and LSPR $\lambda_{\max}$ are gathered for each identified particle and found to be 630 ± 40 nm (n = 1011). Representative single particle spectra are given in Fig. 3c in correspondence with particles identified in colored circles in Fig. 3a. The LSPR $\lambda_{\max}$ of individual gold nanostars in phospholipid nanogel compared to free colloidal gold nanostars within the spectral range from 500–800 nm are summarized with a cumulative distribution function (CDF) in Fig. 3d. The CDF presents the relative number of particles that exhibit maximum scattering at or below a given wavelength and is directly related to the probability of observing particles at that wavelength. A statistically significant red shift is observed for gold nanostars pseudo-immobilized in nanogel compared to free colloidal gold nanostars. A Kolmogorov–Smirnov test indicated a significant difference in scattering behavior between the two populations with a maximum deviation of 22% (p-value 5.0×10^{-23}).

Single particle scattering histograms in Fig. 4 more clearly reveal the distribution of scattering properties for individual

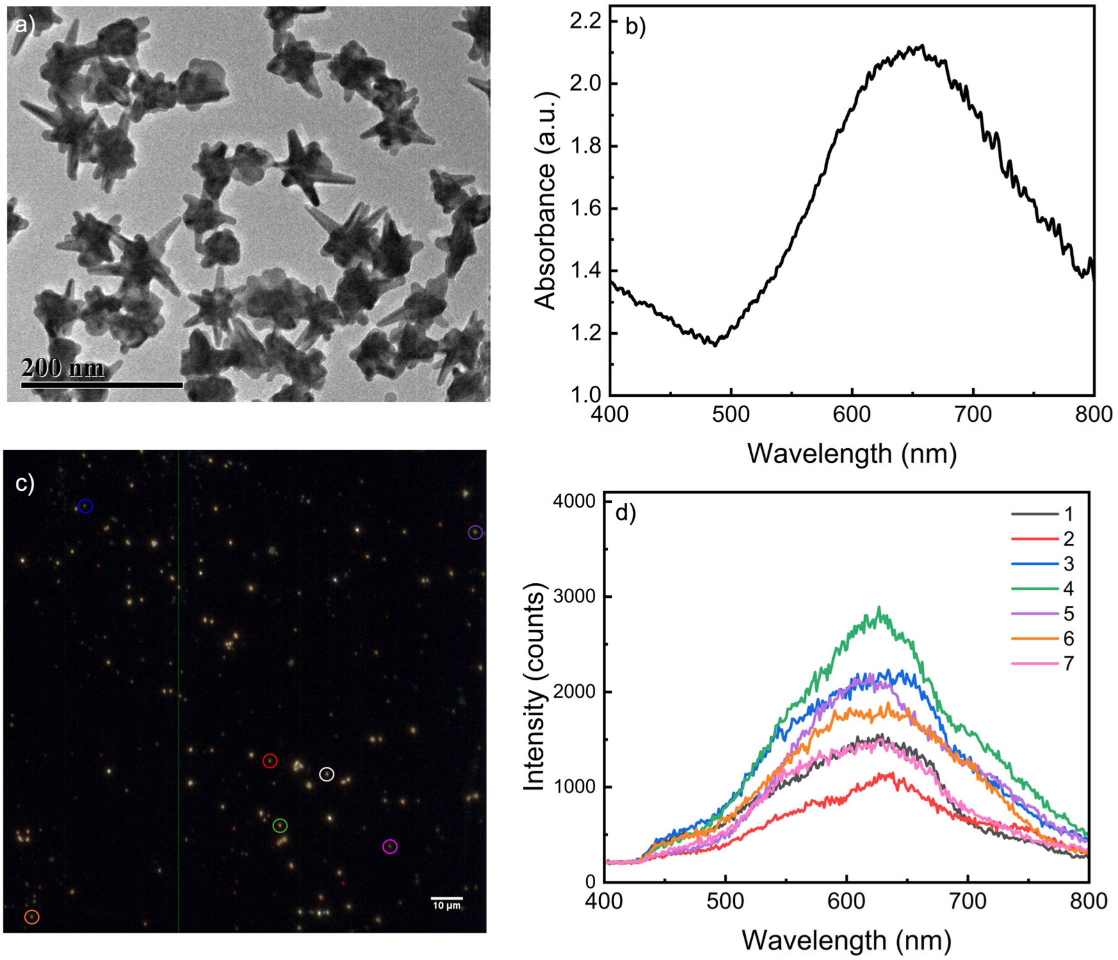

Fig. 2 (a) Transmission electron micrograph for characterization of gold nanostars with an average tip-to-tip diameter of 77.12 nm ± 13.69 (scale bar = 200 nm). (b) A UV-Vis spectrum of nanostars indicates an LSPR λ_{max} of 648 nm (2.1 a.u, 0.229 nM). (c) Hyperspectral DFS image of gold nanostars (scale bar = 10 μm) used for single particle scattering property analysis. (d) Representative single-particle scattering spectra of seven individual nanostars from the population exhibiting LSPR λ_{max} of 610 ± 33 nm (n = 1058).

gold nanostars with and without nanogel. The probability density function provides a theoretical distribution of individual gold nanostar scattering. The area under the curve represents the probability for particles in the corresponding substrate to scatter at a given wavelength. The scattering properties of gold nanostars without nanogel show the highest probability of scattering from 580–640 nm. A red shift is observed in the scattering property analysis of gold nanostars embedded in nanogel, with the highest probability for scattering from 600–660 nm.

The red shift can be explained for numerous reasons, including the convenient dielectric matrix of polymers and plasmonic coupling of nanostars. Previous reports on nanocomposite fabrication have demonstrated that when gold nanostars are present in a chitosan solution, the gold nanostars are stabilized *via* the formation of a surface-protective chitosan layer upon gelation.[9,43] Similarly, herein, the nanogel could serve as an additional protective coating. At low temperatures, gold nanostars are dispersed in a low-viscosity aqueous medium with unentangled phospholipid nanoworms. Upon an increase in temperature, the gold nanostars become stabilized within the gel as the phospholipid structures entangle into a high-viscosity nanogel. This stabilization contributes to an increase in particles retaining an LSPR λ_{max} within 600–700 nm, and a more uniform distribution within this range. At the phase transition temperature where the worm-like structures of self-assembled phospholipids become entangled,[29] the steric effects of the methyl groups in the hydrophobic tails create spatial hindrance and may influence how the gold nanostars are embedded inside the matrix. By creating a spacer between nanostars, the nanogel matrix provides stabilization to prevent aggregation, avoid core-to-core coupling, maintain a uniform particle spacing, and preserve intrinsic hotspot formation. Since the scattering distribution for nanostars embedded in nanogel is a normal distribution with minimal skew, the red shift was broadly observed across many particles rather than a few strong scatterers. This suggests a more uniform plasmonic shift across the substrate

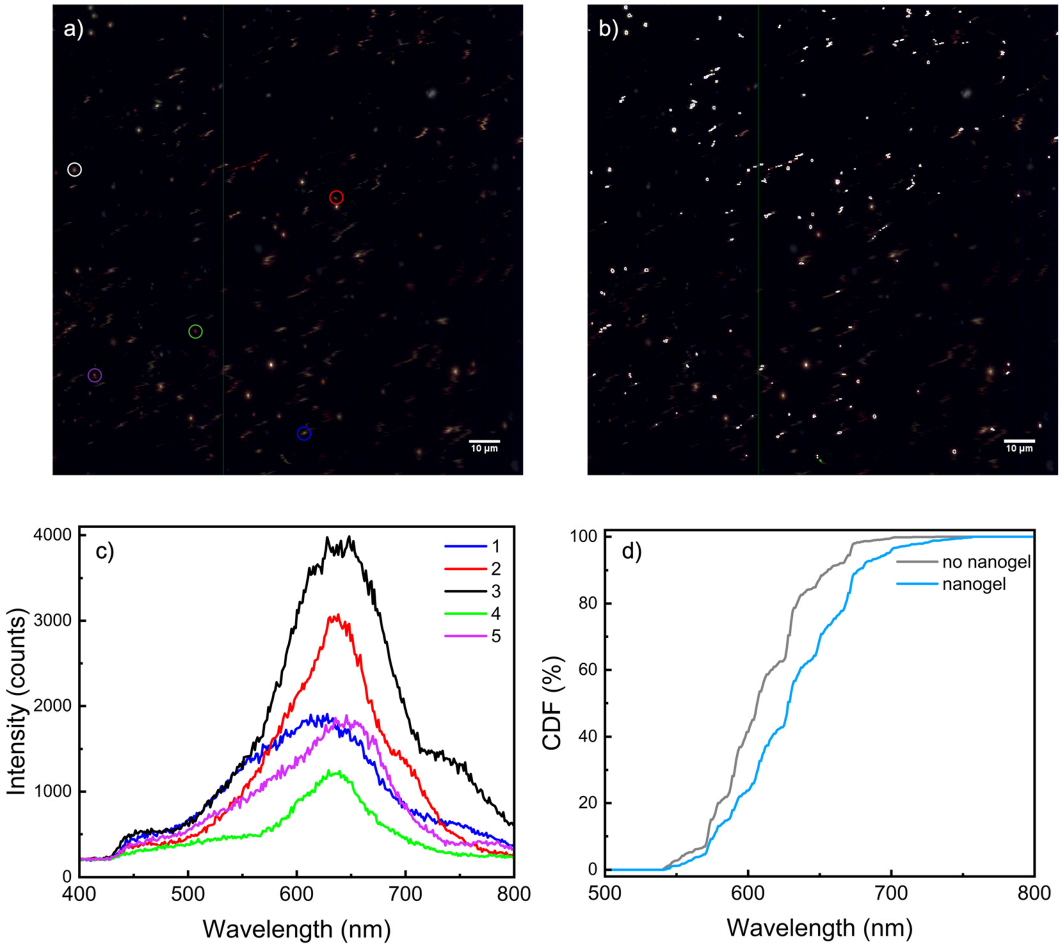

Fig. 3 (a) Dark field image under hyperspectral conditions of gold nanostars in DMPC-DHPC phospholipid nanogel (q = 2.5, 10%), (b) particle filtered image for 1000–5000 counts ≤ 20 pixels (scale bar = 10 microns), (c) representative single particle spectra of nanostars embedded in DMPC-DHPC phospholipid nanogel and (d) cumulative distribution functions from single particle scattering analysis for nanostars embedded in phospholipid nanogel (blue) compared to nanogel-free colloidal gold nanostars.

and potentially some preferential orientation of nanostars within the nanogel matrix. Red shifts are also caused by changing the refractive index and dielectric environment of the media surrounding the nanoparticles.[43,44] Therefore, the change in LSPR $\lambda_{\max}$ observed for the nanogel–nanostar composite can also be attributed to the higher refractive index of the nanogel compared to air or free aqueous solutions.

Finally, the density of nanoparticles can be used to tune plasmonic coupling and control aggregation and can be controlled by changing the final nanoparticle concentration. The nanoparticle concentration will ultimately influence the uniformity of gold nanostar distribution.[9] As the concentration increases, an expected influx of aggregates is anticipated, with $\lambda_{\max}$ red shifted to 700 nm or larger. This is because the aggregation of gold nanostars causes the lengthening of branches and an overall increase in nanostar size.[13,14,41] However, when using a nanogel support, as the volume fraction of gold nanostars increases, the gold nanostars can be forced to move closer together upon transition into high viscosity. Clustering and aggregation are controlled *via* the nanogel matrix, in addition to interparticle orientation. The generalized red shift and plasmonic broadening observed indicate a heterogeneous distribution of morphologies and orientation within a sample.[41] In our study, larger and brighter scatterers were excluded through uniform size and intensity filters to ensure only single-particle spectra were retained for analysis. As a result, these measurements did not directly address concentration-dependent aggregation. However, within the single-particle population analyzed, the probability distribution remained centered at 600–700 nm without strong outliers.

Surface-enhanced Raman scattering of rose bengal using nanostar–nanogel composite

SERS experiments with rose bengal confirmed the viability of the thermally responsive plasmonic nanocomposite as a SERS detection platform. SERS spectra of rose bengal using free colloidal gold nanostars *versus* the nanogel–nanostar composite are presented in Fig. 5a. When using the nanogel–nanostar composite, a 5-fold enhancement in SERS intensity for rose bengal is observed compared to when the nanogel is not

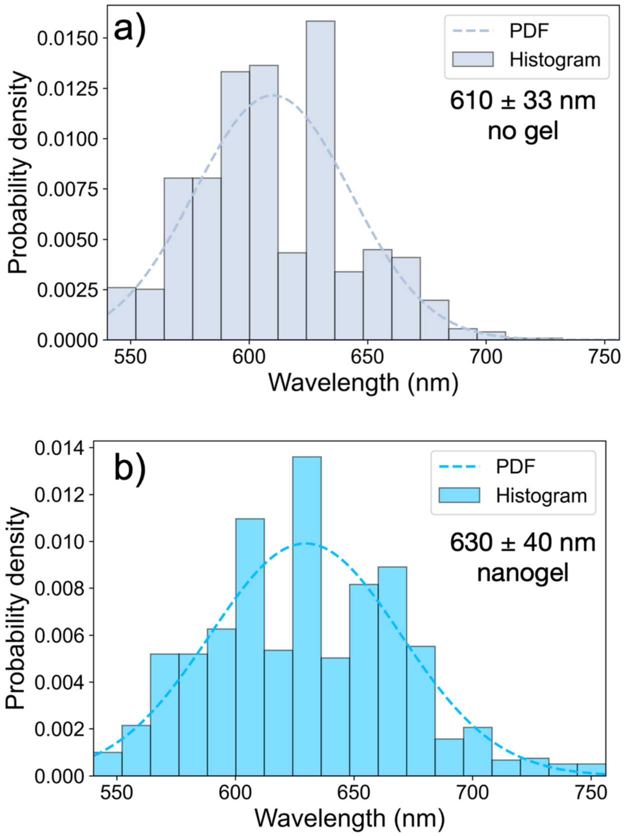

Fig. 4 (a) Histogram with the probability density function (PDF) for single particle analysis of gold nanostars in sodium acetate (n = 1058) and (b) gold nanostars in DMPC-DHPC phospholipid nanogel and (n = 1011).

included (Fig. 5b). The limit of detection was calculated to be 7.4 ± 0.5 nM (LOD = $3s/m$). SERS spectra for determining the detection limit and creating the calibration curve are provided in the SI. Analyses and comparisons were performed using the characteristic peak for rose bengal observed at 1611 cm^{-1} (C=C stretch). Additional peaks at 1266 and 1411 cm^{-1} arise from the PDMS Raman background and are not influenced by the presence of nanogel or nanostar addition. The additional peaks assigned to rose bengal's fingerprint in Fig. 5 are observed in both the colloidal and nanogel conditions and arise from the extended π-conjugation from the stable quinoidal structure.[45] In the colloidal suspension, the heterogeneity of enhancement and overall weak performance leave these weaker Raman bands to fall below the detection limit and appear sporadically, as observed in Fig. S9. The nanogel stabilizes the nanostar orientation and provides a more uniform LSPR environment, allowing the same modes to consistently rise above the noise and appear reproducibly from spot to spot across the substrate (Fig. S10). A comparison of rose bengal SERS response using free colloidal gold nanostar suspensions using higher rose bengal concentrations is provided in the SI to highlight the change in peak appearance is inherently a sensitivity problem.

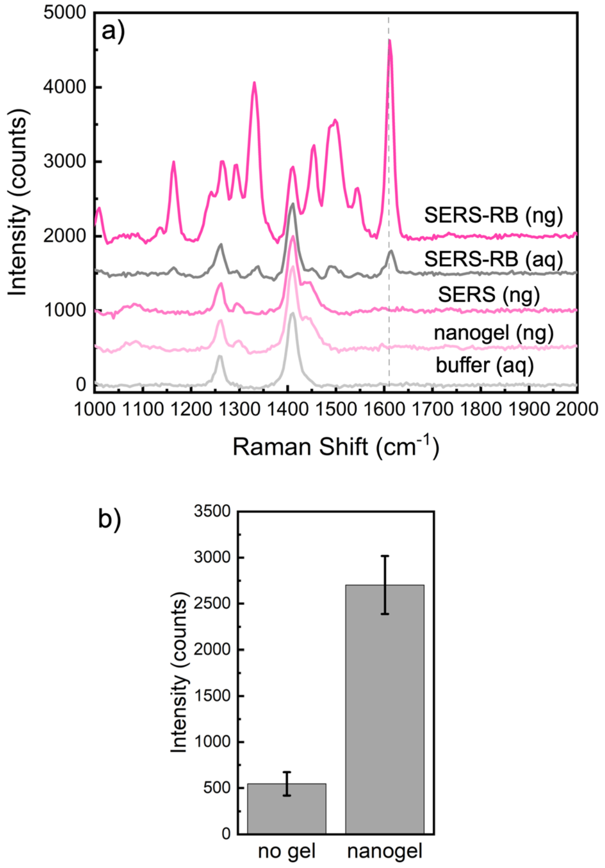

Fig. 5 (a) SERS spectra of 400 nM rose bengal including a blank SERS trace in the nanogel matrix and Raman backgrounds (parameters: 10× obj, range of 400–3600 cm^{-1}, 16 mW, 600 grooves per mm, slit = 200 μm, hole = 100 μm) top-to-bottom: SERS-RB (ng) = rose bengal + nanostars in nanogel matrix; SERS-RB (aq) = rose bengal + nanostars in buffer without nanogel; SERS (ng) = nanostars in nanogel matrix without rose bengal; nanogel (ng) = Raman background for nanogel matrix without stars or analyte; buffer (aq) = Raman background for buffer without stars, analyte or nanogel. Traces were background subtracted using Origin Pro's Peak Analyzer tool and an asymmetric least squares fit. The characteristic rose bengal peak is observed at 1611 cm^{-1}. The additional peaks are from both the PDMS background and additional modes from rose bengal. Peaks at 1266 and 1411 cm^{-1} are attributed to characteristic peaks of the PDMS (channel material) from CH_3 symmetric and asymmetric bending, respectively. The peak at 1299 cm^{-1} and 1440 cm^{-1} arise from a backbone twist and bending in the lipid. However, these peaks are entirely obscured by analyte signal and do not experience enhancement in the presence of nanostars. In addition to the strong characteristic rose bengal peak at 1611 cm^{-1} (symmetric C=C stretching in ring) used for performance comparison, the peaks at 1164 cm^{-1}, 1241 cm^{-1}, 1294 cm^{-1}, 1331 cm^{-1}, 1454 cm^{-1}, ~1490 cm^{-1}, and 1545 cm^{-1} also belong to rose bengal's fingerprint and arise from the ring stretching modes and the xanthene dye framework. (b) Comparison of the SERS intensity for replicate measurements and across at least five distinct spots in the microchannel shows that when nanogel is included to produce a nanogel–nanostar composite, an enhancement in SERS signal is observed relative to nanostars only. The relative standard deviation for SERS using free colloidal gold nanostars was 60% compared to 21% when using the nanogel–star composite as a SERS substrate.

Nanostars are stabilized by the nanogel matrix, resulting in controlled aggregation and particle spacing. As such, it is surprising to see less homogeneity in the rose bengal SERS response in colloidal suspensions, due to the increased rotational freedom that would average out nanoparticle orientation and overall configurational changes. However, the reduced rotational freedom within the gel may contribute to more reproducible local configurations, which could explain the more uniform SERS response observed in nanogel–nanostar systems compared to free colloidal solutions. Nonetheless, it's important to note that preferential orientation effects remain speculative and are only noted here as a potential avenue for future investigation.

The SERS enhancement is attributed, in part, to the controlled spacing of nanostars on a pseudo-immobilized substrate, which resulted in red-shifted and broadened scattering properties compared to nanogel-free measurements. To evaluate spatial variation in the SERS signal spot-to-spot along the microchannel, measurements were acquired in at least five distinct positions within the detection region. Positions were selected without prior identification of scattering intensity *via* darkfield microscopy, as darkfield analyses were only used for optical property investigations and not as a pre-screening tool for SERS. This approach was intended to avoid bias and assess the overall uniformity of the nanostar–nanogel substrate. Based on the nanostar concentration, the estimated nanostar density is on the order of 10^7 nanostars per microliter. This density proved sufficient to yield measurable SERS signals at all tested locations without requiring individual particle localization. Replicate measurements are provided in the SI. Furthermore, nanostars embedded in the phospholipid nanogel afforded a higher precision SERS substrate compared to colloidal platforms with a nearly three-fold reduction in the relative standard deviation for nanocomposite measurements (21% RSD) compared to that of free colloidal nanostars (60% RSD). This is important because, similar to the intensity, the SERS signal should be as uniform as possible across the substrate so that the relative deviation from spot to spot is minimal.[23] Immobilization of a SERS substrate is more reliable because it provides a stable environment for nanoparticles with increased substrate uniformity and reduced aggregation. The uniformity of gold nanostars distributed in a matrix is extremely important in the design of SERS substrates to ensure sensitive and reproducible optical SERS responses.[9] In this work, rose bengal was co-incubated with gold nanostars prior to gelation, such that analyte–substrate interactions were pre-established before nanogel formation and device loading. Post-loading delivery of analyte was not assessed in this initial study but represents an opportunity for further evaluating the dynamic accessibility, reversibility, and reusability of the substrate system for on-demand SERS detection. It is important to note that while the microfluidic device used for these experiments contained 12 parallel channels, all SERS measurements were carried out in a single microchannel. After each sample analysis, the sample-containing SERS substrate was rinsed out of the microchannel, emphasizing the reusability of the microfluidic channel afforded by this thermo-responsive plasmonic substrate. Note that the SERS substrate itself is not reused between samples. Each new sample is loaded with a fresh nanostar–nanogel composite into the clean microchannel, and erasability refers to the capacity to remove and redeposit the nanogel–nanostar substrate between samples.

Conclusions

In this study, gold nanostars were successfully embedded into DMPC-DHPC ($q = 2.5$, 10%) phospholipid nanogels to create a thermally responsive, erasable SERS substrate. The nanogel matrix provided a tunable dielectric environment that stabilized the optical properties of gold nanostars, resulting in a narrower and red-shifted scattering distribution relative to free colloidal nanostars. Single-particle hyperspectral analysis revealed enhanced uniformity in LSPR $\lambda_{\max}$ values, supporting improved reproducibility of SERS response across the substrate. This nanogel–nanostar composite enables reversible immobilization within microfluidic channels, making it an erasable substrate and reusable microchip platform for optical sensing. Importantly, the nanogel substrate itself is not regenerated or recycled, but rather replaced between samples, preserving SERS performance while allowing reuse of the analytical platform. The nanocomposite exhibited a five-fold enhancement in SERS signal intensity and a lower relative standard error compared to nanogel-free suspensions, confirming its viability for sensitive and reliable analyte detection. The novelty of this approach lies in its integration of thermally responsive immobilization with single-particle optical stability, bridging some advantages of colloidal and solid SERS platforms. These features make the platform highly suitable for applications involving microfluidic sensing or lab-on-a-chip diagnostics, where controlled sample flow and reuse of detection zones are critical. The morphological and optical tunability of this nanogel-based system offers broad design flexibility. Future work may focus on optimizing nanostar density, incorporating target-specific surface functionalization, and integrating with other analytical techniques and lab-on-a-chip sample processing to expand the platform's utility in bioanalysis, environmental sensing, and/or real-time diagnostics.

Author contributions

CF was responsible for nanoparticle synthesis and sample preparation; methodology, investigation, validation, and formal analysis for SERS, detection performance, DFS, and single-particle analysis; visualization; and writing the original draft, review & editing. NG was responsible for nanoparticle size analysis and contributed to writing the original draft. LDC was responsible for project administration, funding acquisition, SERS validation, and review & editing.

Conflicts of interest

There are no conflicts to declare.

Data availability

Data supporting this article have been included as part of the supplementary information (SI). Supplementary information is available. See DOI: https://doi.org/10.1039/d5an00833f.

Acknowledgements

The authors acknowledge UNC Charlotte Faculty Research Grant program, UNC Charlotte Academic Affairs, Klein College of Science, and the Chemistry Department for funding this work. The authors thank Most Jannatul Ferdous Suchi for her assistance with PDMS microchip fabrication. The authors thank Maedeh Taghipour and Youxing Chen for their support and assistance with transmission electron microscopy imaging. The authors acknowledge BioRender for Fig. 1 (Created in BioRender. Folks, C. (2025) https://BioRender.com/o2imcne) and the TOC figure (Created in BioRender. Folks, C. (2025) https://BioRender.com/2bzhxdu).

References

1 L. A. Lyon, C. D. Keating, A. P. Fox, B. E. Baker, L. He, S. R. Nicewarner, S. P. Mulvaney and M. J. Natan, Raman Spectroscopy, *Anal. Chem.*, 1998, **70**(12), 341–362, DOI: 10.1021/a1980021p.

2 J. Yi, E.-M. You, R. Hu, D.-Y. Wu, G.-K. Liu, Z.-L. Yang, H. Zhang, Y. Gu, Y.-H. Wang, X. Wang, H. Ma, Y. Yang, J.-Y. Liu, F. R. Fan, C. Zhan, J.-H. Tian, Y. Qiao, H. Wang, S.-H. Luo, Z.-D. Meng, B.-W. Mao, J.-F. Li, B. Ren, J. Aizpurua, V. A. Apkarian, P. N. Bartlett, J. Baumberg, S. E. J. Bell, A. G. Brolo, L. E. Brus, J. Choo, L. Cui, V. Deckert, K. F. Domke, Z.-C. Dong, S. Duan, K. Faulds, R. Frontiera, N. Halas, C. Haynes, T. Itoh, J. Kneipp, K. Kneipp, E. C. Le Ru, Z.-P. Li, X. Y. Ling, J. Lipkowski, L. M. Liz-Marzán, J.-M. Nam, S. Nie, P. Nordlander, Y. Ozaki, R. Panneerselvam, J. Popp, A. E. Russell, S. Schlücker, Y. Tian, L. Tong, H. Xu, Y. Xu, L. Yang, J. Yao, J. Zhang, Y. Zhang, Y. Zhang, B. Zhao, R. Zenobi, G. C. Schatz, D. Graham and Z.-Q. Tian, Surface-Enhanced Raman Spectroscopy: A Half-Century Historical Perspective, *Chem. Soc. Rev.*, 2025, **54**(3), 1453–1551, DOI: 10.1039/d4cs00883a.

3 Z.-Q. Tian, B. Ren, J.-F. Li and Z.-L. Yang, Expanding Generality of Surface-Enhanced Raman Spectroscopy with Borrowing SERS Activity Strategy, *Chem. Commun.*, 2007, (34), 3514–3534, DOI: 10.1039/B616986D.

4 B. Sharma, R. R. Frontiera, A.-I. Henry, E. Ringe and R. P. Van Duyne, SERS: Materials, Applications, and the Future, *Mater. Today*, 2012, **15**(1), 16–25, DOI: 10.1016/S1369-7021(12)70017-2.

5 Y. Liu, H. Yuan, F. R. Kersey, J. K. Register, M. C. Parrott and T. Vo-Dinh, Plasmonic Gold Nanostars for Multi-Modality Sensing and Diagnostics, *Sensors*, 2015, **15**(2), 3706–3720, DOI: 10.3390/s150203706.

6 P. L. Stiles, J. A. Dieringer, N. C. Shah and R. P. Van Duyne, Surface-Enhanced Raman Spectroscopy, *Annu. Rev. Anal. Chem.*, 2008, **1**, 601–626, DOI: 10.1146/annurev.anchem.1.031207.112814.

7 B. Chen, J. Gao, H. Sun, Z. Chen and X. Qiu, Surface-Enhanced Raman Scattering (SERS) Technology: Emerging Applications in Cancer Imaging and Precision Medicine, *Methods*, 2025, **241**, 67–93, DOI: 10.1016/j.ymeth.2025.05.009.

8 L. Shi, Y. Liu, X. Li, H. Zhang, Z. Wang, S. He, D. Fan, X. Huang, Y. Zi, Y. Han, D. Zhang and X. Chen, Advances in Functional Nucleic Acid SERS Sensing Strategies, *ACS Sens.*, 2025, **10**(3), 1579–1599, DOI: 10.1021/acssensors.4c02611.

9 C. Folks, U. S. Phuyal, M. Rajesh, N. Arja, M. Gladden, L. Hamm and A. S. De Silva Indrasekara, Fabrication and Comparative Quantitative Analysis of Plasmonic-Polymer Nanocomposites as Optical Platforms, *Langmuir*, 2021, **37**(44), 12853–12866, DOI: 10.1021/acs.langmuir.1c01826.

10 A. S. D. S. Indrasekara, S. Meyers, S. Shubeita, L. C. Feldman, T. Gustafsson and L. Fabris, Gold Nanostar Substrates for SERS-Based Chemical Sensing in the Femtomolar Regime, *Nanoscale*, 2014, **6**(15), 8891–8899, DOI: 10.1039/C4NR02513J.

11 P. A. Mosier-Boss, Review of SERS Substrates for Chemical Sensing, *Nanomaterials*, 2017, **7**(6), 142, DOI: 10.3390/nano7060142.

12 G.-H. Kim, J. Son and J.-M. Nam, Advances, Challenges, and Opportunities in Plasmonic Nanogap-Enhanced Raman Scattering with Nanoparticles, *ACS Nano*, 2025, **19**(3), 2992–3007, DOI: 10.1021/acsnano.4c14557.

13 A. S. De Silva Indrasekara, S. F. Johnson, R. A. Odion and T. Vo-Dinh, Manipulation of the Geometry and Modulation of the Optical Response of Surfactant-Free Gold Nanostars: A Systematic Bottom-Up Synthesis, *ACS Omega*, 2018, **3**(2), 2202–2210, DOI: 10.1021/acsomega.7b01700.

14 I. B. Becerril-Castro, I. Calderon, N. Pazos-Perez, L. Guerrini, F. Schulz, N. Feliu, I. Chakraborty, V. Giannini, W. J. Parak and R. A. Alvarez-Puebla, Gold Nanostars: Synthesis, Optical and SERS Analytical Properties, *Analysis Sensing*, 2022, **2**(3), e202200005, DOI: 10.1002/anse.202200005.

15 A. Mercedi, F. Cardoni, F. Toffanello, J. Reguera, M. Meneghetti and L. Litti, Reliable Methodology for Measuring SERS Enhancement Factor on Colloidal and Solid Substrates: A Practical Guide, *J. Raman Spectrosc.*, 2025, **56**(9), 835–849, DOI: 10.1002/jrs.6776.

16 K. Kant and S. Abalde-Cela, Surface-Enhanced Raman Scattering Spectroscopy and Microfluidics: Towards Ultrasensitive Label-Free Sensing, *Biosensors*, 2018, **8**(3), 62, DOI: 10.3390/bios8030062.

17 S. Nie and S. R. Emory, Probing Single Molecules and Single Nanoparticles by Surface-Enhanced Raman Scattering, *Science*, 1997, **275**(5303), 1102–1106, DOI: 10.1126/science.275.5303.1102.

18 J. Chen, S. Li, F. Yao, F. Bao, Y. Ge, M. Zou, P. Liang and Q. Chen, Progress of Microfluidics Combined with SERS Technology in the Trace Detection of Harmful Substances, *Chemosensors*, 2022, **10**(11), 449, DOI: 10.3390/chemosensors10110449.

19 K. A. López-Castaños, A. Méndez-Albores and E. Quiroga-González, SERS Strategy for Quantifying Transparent Dry Analytes at Ultra-Low Concentrations Utilizing the Coffee Ring Effect, *Microchem. J.*, 2025, **215**, 114192, DOI: 10.1016/j.microc.2025.114192.

20 K. Ge, Y. Hu and G. Li, Recent Progress on Solid Substrates for Surface-Enhanced Raman Spectroscopy Analysis, *Biosensors*, 2022, **12**(11), 941, DOI: 10.3390/bios12110941.

21 A. de Barros, F. M. Shimizu, C. S. de Oliveira, F. A. Sigoli, D. P. dos Santos and I. O. Mazali, Dynamic Behavior of Surface-Enhanced Raman Spectra for Rhodamine 6G Interacting with Gold Nanorods: Implication for Analyses under Wet versus Dry Conditions, *ACS Appl. Nano Mater.*, 2020, **3**(8), 8138–8147, DOI: 10.1021/acsanm.0c01530.

22 S.-W. Hsu, A. L. Rodarte, M. Som, G. Arya and A. R. Tao, Colloidal Plasmonic Nanocomposites: From Fabrication to Optical Function, *Chem. Rev.*, 2018, **118**(6), 3100–3120, DOI: 10.1021/acs.chemrev.7b00364.

23 G. A. Vinnacombe-Willson, C. García-Astrain, L. Troncoso-Afonso, M. Wagner, J. Langer, P. González-Callejo, D. D. Silvio and L. M. Liz-Marzán, Growing Gold Nanostars on 3D Hydrogel Surfaces, *Chem. Mater.*, 2024, **36**(10), 5192–5203, DOI: 10.1021/acs.chemmater.4c00564.

24 M. R. Bailey, A. M. Pentecost, A. Selimovic, R. S. Martin and Z. D. Schultz, Sheath-Flow Microfluidic Approach for Combined Surface Enhanced Raman Scattering and Electrochemical Detection, *Anal. Chem.*, 2015, **87**(8), 4347–4355, DOI: 10.1021/acs.analchem.5b00075.

25 S. M. Sibug-Torres, D.-B. Grys, G. Kang, M. Niihori, E. Wyatt, N. Spiesshofer, A. Ruane, B. de Nijs and J. J. Baumberg, In Situ Electrochemical Regeneration of Nanogap Hotspots for Continuously Reusable Ultrathin SERS Sensors, *Nat. Commun.*, 2024, **15**(1), 2022, DOI: 10.1038/s41467-024-46097-y.

26 I. J. Jahn, O. Žukovskaja, X.-S. Zheng, K. Weber, T. W. Bocklitz, D. Cialla-May and J. Popp, Surface-Enhanced Raman Spectroscopy and Microfluidic Platforms: Challenges, Solutions and Potential Applications, *Analyst*, 2017, **142**(7), 1022–1047, DOI: 10.1039/C7AN00118E.

27 S. Lian, X. Li and X. Lv, Recent Developments in SERS Microfluidic Chips: From Fundamentals to Biosensing Applications, *ACS Appl. Mater. Interfaces*, 2025, **17**(7), 10193–10230, DOI: 10.1021/acsami.4c17779.

28 B. C. Durney, B. A. Bachert, H. S. Sloane, S. Lukomski, J. P. Landers and L. A. Holland, Reversible Phospholipid Nanogels for Deoxyribonucleic Acid Fragment Size Determinations up to 1500 Base Pairs and Integrated Sample Stacking, *Anal. Chim. Acta*, 2015, **880**, 136–144, DOI: 10.1016/j.aca.2015.03.009.

29 L. A. Holland and L. D. Casto-Boggess, Gels in Microscale Electrophoresis, *Annu. Rev. Anal. Chem.*, 2023, **16**, 161–179, DOI: 10.1146/annurev-anchem-091522-080207.

30 S. Taguchi, K. Suga, K. Hayashi, Y. Okamoto, H.-S. Jung, H. Nakamura and H. Umakoshi, Systematic Characterization of DMPC/DHPC Self-Assemblies and Their Phase Behaviors in Aqueous Solution, *Colloids Interfaces*, 2018, **2**(4), 73, DOI: 10.3390/colloids2040073.

31 S. A. Archer-Hartmann, L. M. Sargent, D. T. Lowry and L. A. Holland, Microscale Exoglycosidase Processing and Lectin Capture of Glycans with Phospholipid Assisted Capillary Electrophoresis Separations, *Anal. Chem.*, 2011, **83**(7), 2740–2747, DOI: 10.1021/ac103362r.

32 T. J. Pappas and L. A. Holland, Fluid Steering in a Microfluidic Chip by Means of Thermally Responsive Phospholipids, *Sens. Actuators, B*, 2008, **128**(2), 427–434, DOI: 10.1016/j.snb.2007.06.031.

33 L. D. Casto-Boggess, L. A. Holland, P. A. Lawer-Yolar, J. A. Lucas and J. R. Guerrette, Microscale Quantification of the Inhibition of Neuraminidase Using Capillary Nanogel Electrophoresis, *Anal. Chem.*, 2022, **94**(46), 16151–16159, DOI: 10.1021/acs.analchem.2c03584.

34 J. O. Mills and L. A. Holland, Membrane-Mediated Capillary Electrophoresis: Interaction of Cationic Peptides with Bicelles, *Electrophoresis*, 2004, **25**(9), 1237–1242, DOI: 10.1002/elps.200405879.

35 S. A. Archer-Hartmann, C. L. Crihfield and L. A. Holland, Online Enzymatic Sequencing of Glycans from Trastuzumab by Phospholipid-Assisted Capillary Electrophoresis, *Electrophoresis*, 2011, **32**(24), 3491–3498, DOI: 10.1002/elps.201100432.

36 J. Turkevich, P. C. Stevenson and J. Hillier, A Study of the Nucleation and Growth Processes in the Synthesis of Colloidal Gold, *Discuss. Faraday Soc.*, 1951, **11**(0), 55–75, DOI: 10.1039/DF9511100055.

37 M. M. Vega, A. Bonifacio, V. Lughi, S. Marsi, S. Carrato and V. Sergo, Long-Term Stability of Surfactant-Free Gold Nanostars, *J. Nanopart. Res.*, 2014, **16**(11), 2729, DOI: 10.1007/s11051-014-2729-z.

38 P. F. Gao, G. Lei and C. Z. Huang, Dark-Field Microscopy: Recent Advances in Accurate Analysis and Emerging Applications, *Anal. Chem.*, 2021, **93**(11), 4707–4726, DOI: 10.1021/acs.analchem.0c04390.

39 P. Zamora-Perez, D. Tsoutsi, R. Xu and P. Rivera_Gil, Hyperspectral-Enhanced Dark Field Microscopy for Single and Collective Nanoparticle Characterization in Biological Environments, *Materials*, 2018, **11**(2), 243, DOI: 10.3390/ma11020243.

40 C. L. Nehl, H. Liao and J. H. Hafner, Optical Properties of Star-Shaped Gold Nanoparticles, *Nano Lett.*, 2006, **6**(4), 683–688, DOI: 10.1021/nl052409y.

41 C. G. Khoury and T. Vo-Dinh, Gold Nanostars For Surface-Enhanced Raman Scattering: Synthesis, Characterization and Optimization, *J. Phys. Chem. C*, 2008, **112**(48), 18849–18859, DOI: 10.1021/jp8054747.

42 C. Novo, A. M. Funston, I. Pastoriza-Santos, L. M. Liz-Marzán and P. Mulvaney, Influence of the Medium Refractive Index on the Optical Properties of Single Gold Triangular Prisms on a Substrate, *J. Phys. Chem. C*, 2008, **112**(1), 3–7, DOI: 10.1021/jp709606u.

43 D. S. Dos Santos, P. J. G. Goulet, N. P. W. Pieczonka, O. N. Oliveira and R. F. Aroca, Gold Nanoparticle Embedded, Self-Sustained Chitosan Films as Substrates for Surface-Enhanced Raman Scattering, *Langmuir*, 2004, **20**(23), 10273–10277, DOI: 10.1021/la048328j.

44 H. A. Vienna, C. R. Klimpovuz, D. A. Turchetti, A. L. Rossi, M. M. Oliveira, A. Marletta and L. C. Akcelrud, Polyfluorene-Based Conjugated Nanocomposites with in Situ Gold Nanoparticles: Synthesis via Rational Chemical Passivation and Characterization of Supramolecular Fibrillar Structures, *J. Mol. Struct.*, 2025, **1322**, 140431, DOI: 10.1016/j.molstruc.2024.140431.

45 H. R. Zhu and L. Parker, A Spectroscopic Study of Rose Bengal, *Chem. Phys. Lett.*, 1989, **162**(6), 424–430, DOI: 10.1016/0009-2614(89)87002-2.